



**Connecting Charge Transfer Kinetics to Device Parameters  
of a Narrow-bandgap Polymer-based Solar Cell**

Journal:	<i>Physical Chemistry Chemical Physics</i>
Manuscript ID	CP-ART-07-2016-004688.R1
Article Type:	Paper
Date Submitted by the Author:	21-Aug-2016
Complete List of Authors:	Song, Jongwoo; Konkuk University, Chemistry Lee, Younah; Konkuk University, Chemistry Jin, Boa; Konkuk University, Chemistry An, Jongdeok; Konkuk University, Konkuk University - Fraunhofer Institute for Solar Energy Systems Next Generation Solar Cell Research Center Park, Hyunmin; Konkuk University, Chemistry Park, Hoon; Konkuk University, Konkuk University - Fraunhofer Institute for Solar Energy Systems Next Generation Solar Cell Research Center Lee, Myoung Hee; Konkuk University, Konkuk University - Fraunhofer Institute for Solar Energy Systems Next Generation Solar Cell Research Center Im, Chan; Konkuk University, Chemistry; Konkuk University, Konkuk University - Fraunhofer Institute for Solar Energy Systems Next Generation Solar Cell Research Center



## Physical Chemistry Chemical Physics

## ARTICLE

## Connecting Charge Transfer Kinetics to Device Parameters of a Narrow-bandgap Polymer-based Solar Cell

Received 00th January 20xx,  
Accepted 00th January 20xx

DOI: 10.1039/x0xx00000x

[www.rsc.org/](http://www.rsc.org/)

Jongwoo Song<sup>a</sup>, Younah Lee<sup>a</sup>, Boa Jin<sup>a</sup>, Jongdeok An<sup>b</sup>, Hyunmin Park<sup>a</sup>, Hoon Park<sup>b</sup>, Myounghee Lee<sup>b</sup> and Chan Im<sup>a, b, \*</sup>

To achieve intrinsically light-weight flexible photovoltaic devices, a bulk-heterojunction-type active layer with a narrow-bandgap polymer is still one of the most important candidates. Therefore, detailed information about the charge transfer efficiency from a photo-excited species on an electron-donating polymer to an electron acceptor is an important factor given that it is among the most fundamental quantitative measures to understand the solar power conversion efficiency in particular at the initial stage followed by primary exciton formation. To obtain accurate information in this regard, wide-range acceptor concentration-dependent transient absorption spectroscopy with femtosecond laser pulse excitation was performed by using a representative narrow-bandgap polymer, commonly known as PTB7. Investigated acceptor concentration range was covered from 0.01 wt% up to 10 wt% in addition to a 0 wt% pristine polymer sample and a sample with a conventional acceptor concentration of 60 wt%, which is important for high efficiency. From that kinetic data, almost two orders of magnitude faster acceptor-induced charge transfer rate constant in addition to the native primary exciton lifetime of about 100 picoseconds could be extracted. Those data were used to verify the suggested kinetic model and compared with device properties that shows no meaningful loss during extraction of photo-generated charge carriers.

### Introduction

Narrow-bandgap (NBG) polymers are still believed to be an important candidate for use as an active layer component of soluble polymeric bulk-heterojunction (BHJ) solar cells as significantly higher power conversion efficiency (PCE) of these polymers has been reported.<sup>1,2,3</sup> Although the PCE of an NBG polymer close to 10% is not yet comparable with market-dominating silicon-based solar cells, the polymer has shown an impressive possibility not only for light-weight flexible photovoltaic (PV) devices but also for promising printable electronics due to its intrinsic compatibility with high throughput solution process.<sup>4</sup>

To prepare an efficient PV device with a NBG polymer, a proper counterpart, typically a fullerene derivative, is used, which is known as an effective electron acceptor which forms an optimum BHJ active layer where incident photons are absorbed and subsequently transformed to free charge carriers (CCs) rather than recombining mono-molecularly. In fact, acceptor-induced efficient charge transfer (CT) can be easily confirmed by measuring of efficient photoluminescence

(PL) reduction upon adding of a fullerene derivative into, for instance, a poly-3-hexylthiophene (P3HT) solid. Furthermore, acceptor-induced CT rate constant can be estimated even by means of acceptor concentration dependent steady-state PL spectroscopy, as shown with a comparable  $\pi$ -conjugated polymer blend system previously.<sup>5</sup>

Problems arose when a polymer system has very low photoluminescence quantum yield (PLQY) as for the case of some NBG polymers such as PCPDTBT.<sup>6</sup> In this case, so-called transient absorption spectroscopy (TAS) must be performed to depict the nonradiative exciton dynamics, including the CT. TAS enables the population of both radiative and nonradiative excited species to be detected, including primary singlet excitons, triplet excitons, or bound electron and hole pairs. Numerous TAS studies have been conducted related to organic solar cell (OSC), including a comprehensive review of TAS that deals with many specific aspects related to P3HT-based OSCs.<sup>7</sup> However, the reason to use TAS is not only the difficulty of PL signal detection but also the amplitude mismatch between PLQY and the device's external and internal quantum efficiency (EQE and IQE, respectively). As mentioned, the PCPDTBT has a significantly low intrinsic PLQY of approximately 6%<sup>6</sup> from PCPDTBT's pristine film while IQE of PCPDTBT's optimized device is more than 80%.<sup>8</sup> The important point here is that the both PLQY and IQE are actually ratios calculated similarly based on the same total numbers of absorbed photon in an active layer, i.e., the former is the ratio of the emitted photon numbers and the latter is that of the

<sup>a</sup> Department of Chemistry, Konkuk University, 120 Neungdong-ro, Gwangjin-gu, Seoul 143-701, Korea.

<sup>b</sup> Konkuk University – Fraunhofer Institute for Solar Energy Systems Next Generation Solar Cell Research Center (KFNSC), Konkuk University, 120 Neungdong-ro, Gwangjin-gu, Seoul 143-701, Korea.

Electronic Supplementary Information (ESI) available: See DOI: 10.1039/x0xx00000x

photogenerated electron numbers normalized to the same basis. This means that the high IQE cannot be explained when the CC photogeneration is described only as a competitive process to the PL emission process. This is also valid for a well-studied P3HT system although its PLQY is significantly larger than that of PCPDTBT or similar NBG polymers. Pristine samples have a PLQY of approximately 33%,<sup>9</sup> which is clearly smaller than its EQE, often denoted as the incident photon-to-current conversion efficiency (IPCE), and is smaller again than the reported IQEs of most optimized devices.<sup>7</sup>

Consequently, CT from donor to acceptor has to be considered at least as a competitive process against all mono-molecular instantaneous relaxation processes including nonradiative as well as radiative processes. Hence, the TAS or similar methods to depict nonradiative latent processes are important to evaluate active materials for PV applications. Therefore, many NBG polymers including PCPDTBT, the predecessor of the higher PCE having PTB7, and PTB7 itself with a numbers of other NBG derivatives were often studied by means of various kinetic studies including TAS. Clarke et al. have shown the influences of dithiol additive for PCPDTBT by TAS up to millisecond time range.<sup>10</sup> Jarzab et al. have reported 0.04% PLQY with voltage bias and temperature-dependent PL decay kinetics of PCPDTBT blend samples.<sup>6</sup> In addition, Mikhnenko et al. have presented about PCPDTBT's exciton diffusion length of about 10.5 nm by using PL decay kinetics.<sup>11</sup> Various NBGs' exciton dynamics to clarify effects of chemical structures on PV properties also by using TAS with fs laser pulses were shown by Tautz et al.<sup>12</sup> Furthermore, Granzini et al. have shown additional TAS with extremely short laser pulses.<sup>13</sup> Recently, similar kinetics studies with various NBG derivatives were also reported.<sup>14–16</sup> The intensive studies about PCPDTBT are due to the fact that it was the first NBG polymer to successfully overcome the PCE limit of P3HT. Helpful reviews about the synthesis of the conjugated polymers for organic PV applications<sup>17</sup> and the strategy to improve the PCE of BHJ solar cells<sup>18</sup> are mentioned here for better overview.

Shortly after the successful début of PCPDTBT, further improved PTB7 was introduced and followed by numerous time-resolved spectroscopic studies, for instance, by Carsten et al. with a conventional TAS method.<sup>19</sup> Soon et al. have shown a TAS study with PTB7, especially for its correlation with triplet population and character.<sup>20</sup> Herdley et al. have shown acceptor concentration-dependent PL decay mainly to discuss about optimum morphology of that system.<sup>21</sup> Later, a comprehensive TAS study on the PTB7 neat and blend systems was presented by Szarko et al.<sup>22</sup> Recently, Gerhard et al. have reported a study about CT states by temperature- and energy-dependent near infrared emission.<sup>23</sup>

In spite of the above-mentioned intensive efforts and valuable contribution in order to understand the complicated exciton dynamics of NBG polymers, connecting the exciton dynamics of those solid systems to their corresponding device properties is difficult; in other words, connecting the kinetic parameters to their short-circuit current ( $J_{sc}$ ) values or IQEs in a strictly quantitative way is difficult. The quantitative connection between kinetic parameters and device properties is

important not only for understanding the underlying mechanisms of BHJ organic PV devices but also for the verification of the meaning and value of those time-consuming time-resolved kinetic studies on active materials. Simultaneously, such parametric correlations should also be essential for removing any ambiguities caused by the complexity of kinetic behaviours, in particular within such disordered random solids. These are undoubtedly essential not only for the expansion of scientific knowledge but also for the improvement of practical performances of those materials for PV applications.

Therefore, we have decided to investigate a representative NBG polymer, PTB7, by means of an acceptor concentration-dependent TAS. Covering concentration range was from 0.01 wt%–60 wt% including a neat sample in order to extract reliable acceptor-induced CT rate constant, primary exciton decay lifetime, and subsequent recombination kinetics that occur afterwards. At the same time, typical BHJ devices were prepared and characterized for the same concentration under the same active-layer deposition condition to keep consistency. Later, those kinetic parameters were used to calculate the possible numbers of photogenerated electron and hole pairs for a given acceptor concentration in order to compare those values with their corresponding device parameters. Finally, the validity of the suggested scheme for various excited species and their dynamics were discussed by using a strictly limited reaction kinetic framework rather than technical fitting with multi-exponential parameters. It should be noticed that the concentration range used in this study is focused mainly for the range between 0.01% and 10% which is lower than that of usual device preparation condition because that range being covered three orders of magnitude is more important to depict precise exciton dynamics for the target system.

## Experimental

### Preparation

All chemicals including poly[4,8-bis((2-ethylhexyl)oxy)benzo[1,2-*b*:4,5-*b'*]dithiophene-2,6-diyl][3-fluoro-2-[(2-ethylhexyl)carbonyl]thieno[3,4-*b*]thiophenediyl] (PTB7, 1-Material Inc.) and [6,6]-phenyl-C<sub>71</sub>-butyric acid methyl ester (PC<sub>71</sub>BM, 1-Material Inc.)—an electron donor and an electron acceptor—were used as purchased without any further purification.

All devices were prepared as described in the earlier study<sup>22</sup> except the effort to keep all active layer thickness as identical as possible given that one of the main purposes of this study is to depict the relation between acceptor concentration dependency of their spectroscopic kinetics and that of their device parameters, fill factors (FF), open-circuit voltages ( $V_{oc}$ ), short-circuit current densities ( $J_{sc}$ ), and PCEs. The structure of prepared devices is typically as follows: “glass(1.1 mm)/ITO (180 nm)/PEDOT:PSS(50 nm)/PTB7:PC<sub>71</sub>BM(100 nm)/LiF(0.3 nm)/Al(120 nm).”

In addition, single-layer samples on glass substrates for diverse optical characterizations were prepared in a similar manner as

that of ITO-covered glass substrates for device preparation as described previously<sup>24</sup> to maintain the film quality as much as possible. In this study, the concentration of solutes, namely total weight concentration of PTB7 and PC<sub>71</sub>BM together, was 2.16 wt% in chlorobenzene (CB) solvent. Each PC<sub>71</sub>BM concentration in total blend solutes were 0.01, 0.03, 0.1, 0.3, 1.0, 3.0, 10, 60 wt% to obtain wide-range acceptor concentration dependency for accurate spectroscopic kinetics. Thin films were deposited on substrates by conventional spin-coating at revolution-per-minute (RPM) values ranging from 6,500 for 0.01 wt% to 5,000 for 10 wt%. The RPM values were varied to keep thicknesses as same as possible for all samples used. After the deposition of those active layers on substrates, either on bare glasses or ITO-covered glasses, they were encapsulated with engraved cover glasses to prevent any possible degradation problems during measurement.

### Characterization

UV-visible absorption (UV-Vis) spectra as well as transmittance spectra of solution samples and films spin-coated on glass substrates were recorded with a spectrophotometer (Nenosys-2000, Scinco). Additional reflectance spectra were measured with a spectrophotometer (AvaSpec-ULS2048, Avantes) especially for device samples with Al top electrode due to their opacity. Steady-state fluorescence spectra both for a solution and films were measured by using a spectrophotometer (FS-2, Scinco) equipped with a 150 W Xenon lamp as an excitation light source. Absolute PLQYs were obtained by using a commercial system (Quantaaurus-QY, C11347, Hamamatsu Photonics K.K.).

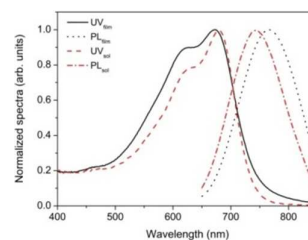
The ultrafast transient absorption spectroscopy (TAS) was performed by utilizing a Ti:sapphire regenerative amplifier laser system (Libra, Coherent) with a pulse width of approximately 100 fs at a repetition rate of 1 kHz in conjunction with a pump-probe spectrometer (Helios, Ultrafast Systems LLC). To select a specific excitation wavelength, an optical parametric amplifier system (TOPAS, Coherent) was used. For white light continuum to probe excited species, a sapphire crystal was used. The TAS kinetics was measured up to 3 nanoseconds (ns) with picosecond (ps) time-resolution and the probing wavelength ranges were covered from 450 to 900 nm for a visible (Vis) wavelength range detector and 900 nm to 1,400 nm for an IR wavelength range detector. The above-mentioned detection ranges were given for optimal signal to noise ratio (S/N) cases. Often there was a gap between approximately 800 nm and 900 nm where there was not sufficient S/N available, especially under a low excitation intensity situation. In most cases, three different intensities (200  $\mu\text{J}/\text{cm}^2$ , 80  $\mu\text{J}/\text{cm}^2$ , 30  $\mu\text{J}/\text{cm}^2$ ) of the pump beam per pulse were used to perform TAS. The average size of pump beams was approximately 1 mm in diameter. This value is relatively larger than the other conventional TAS cases because we were trying to reduce too strong intensity-dependent bimolecular behaviours by decreasing photon flux density because such strong bimolecular influences can affect the patterns of native kinetic behaviours. TAS spectra were

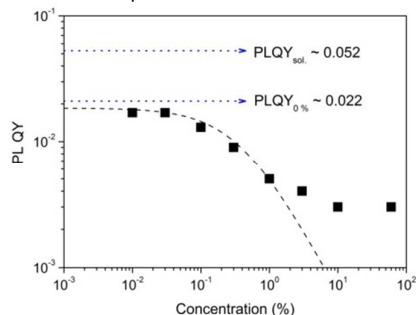
recorded as the change of absorbance ( $\Delta A$ ) by using a personal computer and a program provided by the manufacturer of the pump-probe spectrometer.

PCE values with device parameters, FF,  $V_{\text{OC}}$ , and  $J_{\text{SC}}$  were estimated carefully according to a conventional standard condition as described in detail previously.<sup>24</sup> Thicknesses of active layers were measured primarily by using a surface profiler (XP-200, AMBios) and later the values were verified with the results obtained from an atomic force microscope (XE-70, Park systems), typically under noncontact mode. The data were also cross-checked with reflectance data of devices to prevent any significant deviation in film thickness, especially between semi-transparent single-layer samples and opaque device samples.

### Results and discussion

Steady-state UV-Vis and PL spectra of a diluted solution in CB and a thin pristine film are shown in Figure 1. PL spectra were performed with an excitation wavelength of 660 nm. A significant change by solidification was that the maximum PL peak at 767 nm of a pristine film was red-shifted about 70 meV compared to that of the solution at 743 nm as is usual in  $\pi$ -conjugated polymers due to enhanced  $\pi$ - $\pi$  interaction<sup>25</sup> and/or extension of effective  $\pi$ -conjugation length<sup>26</sup> under densely packed situation. However, the maximum UV-Vis peak of a pristine film was marginally blue-shifted to 672 nm from that at 678 nm of a solution sample, and this is unusual compared to the red-shift that occurs upon solidification. Furthermore, both secondary shoulder peaks of the solution and film samples were similarly centred at approximately 626 nm. The unchanged or marginally blue-shifted feature in UV-Vis can be explained by using the term of forbidden state formation for energetically low-lying state having extended  $\pi$ -conjugation. If only a transition to next higher energy level is allowed, then a blue-shifted band can be observed.<sup>27</sup> The fine structures with more than two peaks both in UV-Vis spectra of the solution and film had approximately 140 meV differences and this is a reasonable value to assign that as a vibrational structure caused by a C=C double bond stretching mode. The values of the full width at half maximum (FWHM) of approximately 250 meV was virtually the same for each PL band of a solution and a film sample. The FWHM of approximately 250 is also similar for the first UV-Vis band of a solution sample while the first UV-Vis band of a film sample seems approximately 40 meV broadened.



**Figure 1.** UV-Vis and PL spectra of a PTB7 solution in CB and a film.**Figure 2.** Steady-state PLQY plot as a function of acceptor concentration.

The difference in UV-Vis caused by solidification can be described as an inhomogeneous broadening of the native FWHM value of a solution sample. In fact, the observed inhomogeneous broadening of the UV-Vis band upon solidification is also a sign of the significant interaction between polymer chains and subsequent increasing of energetic disorder of the solid system.<sup>28</sup> It is noteworthy that the shifts in PL and UV-Vis of the P3HT:PC<sub>61</sub>BM system were approximately 0.5 eV.<sup>29</sup> This value being an order of magnitude larger than that of the PTB7:PC<sub>71</sub>BM system reflects the difference between pronounced molecular ordering facilities of the regioregular P3HT.<sup>30</sup>

Obtained PLQYs excited at 660 nm of solution and pristine film samples were about 5.2 and 2.2%, respectively. The value of a pristine film is comparable with the value of 0.02 reported by Hedley et al.<sup>21</sup> This implies that the intrinsic PLQY of PTB7 is much lower than usual  $\pi$ -conjugated polymer materials even in a dilute solution; in other words, PTB7 has inherently very efficient nonradiative decay channels. The reduction of PLQY from a solution to a film is a typical feature of  $\pi$ -conjugated polymeric solids due to enhanced PL quenching probability caused by three-dimensional (3D) dense packing of polymer chains.<sup>6</sup> In spite of the low PLQY, systematic reduction of PLQY as a function of acceptor concentration was observed, as shown in Figure 2. PLQY was reduced almost an order of magnitude, from 2.2% down to 0.3%, upon the addition of 10 wt% acceptor into the narrow-bandgap polymer matrix.

By using the basic Stern–Volmer formalism with Equation (1),<sup>32</sup> the PL quenching rate constant can be extracted from the acceptor concentration-dependent PLQY data.

$$\frac{\varphi_{f,0}}{\varphi_f} = 1 + \tau_0 k_{Q(PL)} [Q], \quad (1)$$

where  $\varphi_f$  is the PLQY at a given acceptor (quencher) concentration;  $\varphi_{f,0}$  is the PLQY at 0 wt% of acceptor concentration;  $\tau_0$  is the intrinsic lifetime of the given NBG polymer solid system;  $k_{Q(PL)}$  is the PL quenching rate constant;  $[Q]$  is a given quencher concentration. It should be noted that Equation (1) was slightly modified and plotted to compare with

the nonnormalized experimental PLQYs, as shown in Figure 2. The obtained value of  $k_{Q(PL)}$  was about  $1.8 \times 10^{13} \text{ s}^{-1}$  by using a  $\tau_0$  of 100 ps extracted from the TAS kinetics discussed later in this study. This value is almost an order of magnitude larger than the value of  $3.2 \times 10^{12} \text{ s}^{-1}$  for the PPV:TNF system.<sup>5</sup>

However, the experimental PLQY values follow the calculated theoretical curve only up to approximately 1 wt%, as shown in Figure 2. Interestingly,  $k_{Q(PL)}$  for acceptor concentration higher than 1.0 wt% seems less effective than that for a lower acceptor concentration range. This is attributed to the pronounced phase separation-induced change of morphology, which is typical for analog BHJ systems, especially with higher acceptor concentration as reported earlier.<sup>21</sup> Such systems can exhibit severe deviation from well-dispersed mixture systems such as the solution for which the original Stern–Volmer formalism was derived.<sup>32</sup> It should be also noted that technical limits during absolute PLQY measurement can be reached when the PLQY's value is close the order of  $10^{-3}$ .

In Figure 3, current density–voltage (J–V) plots of devices with various acceptor concentrations are shown. From the plots, PV device parameters are extracted and plotted in Figure 4 as functions of acceptor concentration and are summarized in Table 1. The acceptor concentration-dependent PCE trend has virtually the same functional dependence with  $J_{SC}$ . FF has also a similar trend as PCE but decreases slightly up to approximately 0.1 wt% and then stays constant up to approximately 10 wt% with a value of approximately 25%. Subsequently, FF increases about two-fold from 10 wt% to 60 wt% where the PTB7:PC<sub>71</sub>BM device reaches the highest PCE as reported in many previous reports.<sup>1,33</sup> However, a dramatically different dependency was observed with  $V_{OC}$ .  $V_{OC}$  was virtually constant with a value of approximately 1.1 V from 0.01 to 0.1 wt% and then decreased monotonically with increasing acceptor concentration.  $J_{SC}$  from 3 wt% to 60 wt% increased about two orders of magnitude whereas  $J_{SC}$  from 0 wt% to 3 wt% increased only about two-fold. As a result, PCE increased from 3 wt% very rapidly as PCE is a product of  $J_{SC}$ ,  $V_{OC}$ , and FF. It might be helpful to notice that both PCE and  $J_{SC}$  are presented in the logarithmic scale while FF and  $V_{OC}$  are presented in the linear scale.

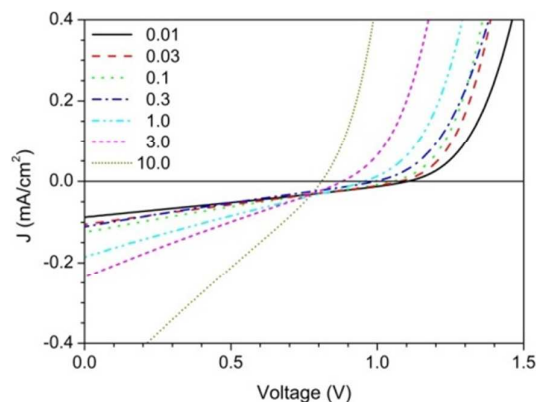


**Figure 3.** J–V characteristics of used devices with various acceptor concentrations.

**Table 1.** Estimated photovoltaic device parameters at various acceptor concentrations.

Acceptor concent. (%)	$V_{OC}$ (V)	$J_{SC}$ ( $\text{mA}/\text{cm}^2$ )	FF (%)	PCE (%)	$R_{sh}$ ( $\Omega\text{-cm}^2$ )	$R_s$ ( $\Omega\text{-cm}^2$ )
0.0	1.2	0.090	31.3	0.033	16,324	2,765
0.01	1.1	0.083	27.6	0.027	13,888	5,684
0.03	1.1	0.106	25.2	0.029	9,990	5,480
0.1	1.1	0.125	23.7	0.031	7,445	5,508
0.3	0.99	0.112	23.9	0.026	7,882	6,251
1.0	0.96	0.185	23.8	0.042	4,626	3,842
3.0	0.87	0.231	24.6	0.049	3,537	2,933
10	0.81	0.551	24.8	0.111	1,399	991
60	0.72	16.0	52.9	6.1	259	8.5

The gradual decrease of  $V_{OC}$  with increasing acceptor concentration should reflect that the  $V_{OC}$  depends on the accumulation of photogenerated CCs inside the BHJ active layer because of insufficient CC transport facility below approximately 10 wt% range. This can be also supported by the fact that the exponentially increasing acceptor concentration dependency of  $J_{SC}$  in the 3–10 wt% range, despite the spectroscopic results strongly supporting that the CC, or at least bound electron and hole pairs that can be referred as precursors of free CCs, and generation at moderate acceptor concentration is already reached on a significant level, as discussed in the later part of this study. At the same time, the two-fold increasing of FF above 10 wt% is also strong evidence that the bipolar CC transport inside the active layer is more improved due to optimal morphology formation above 10 wt%. Analog CC generation and transport facility depend on acceptor concentration was also reported with a polyphenylenevinylene copolymer solid and a hexa-*peri*-hexabenzocoronene solid, each blended with perylene-3,4,9,10-tetracarboxylic diimide.<sup>34</sup> Expectedly, device behaviors of P3HT:PC<sub>61</sub>BM and P3HT:ICBA was also comparable, especially for the low concentration range.<sup>29</sup>

Similar interpretation about the enhanced CC mobility above proper acceptor concentration was already suggested in our previous study dealing with thickness-dependent IQE of the same BHJ system<sup>24</sup> For the same composition of PTB7 and PC<sub>71</sub>BM for the active layers with approximately 90 nm thicknesses, the obtained PCEs were higher than 6% and the corresponding IQEs were also higher than 70% virtually over the entire spectral range of photon absorption. Even for the less efficient device with 320 nm thickness, its PCE was 2.2% and IQE was approximately 20%. This means that approximately only 2% of the PE population that decays

radiatively cannot be a major source of photogenerated CCs at all.

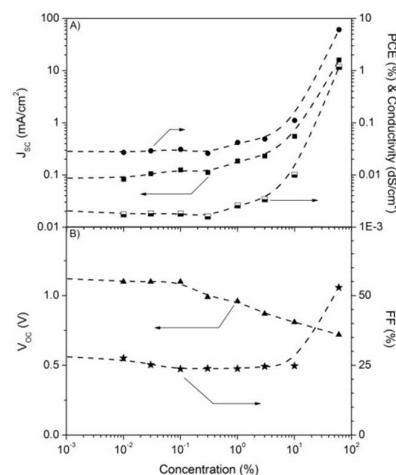
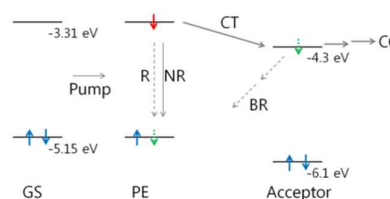


**Figure 4.** PV device parameters; A)  $J_{SC}$ , PCE, and conductivity, B)  $V_{OC}$  and FF, plotted as functions of acceptor concentration. Dashed lines are for eye-guiding purpose.



**Scheme 1.** Energy-level diagram for overview.

To discuss about the TAS results, it might be helpful to define crucial states to describe the exciton dynamics within the active layers, as shown in Scheme 1. For that, simple two-state models were used for both PTB7 and PC<sub>71</sub>BM to obtain a clear kinetic overview. After the absorption of incident photons, primary excitons (PEs) are generated. These PEs can return to their ground states (GSs) through either radiative (R) or nonradiative (NR) decays, assuming that extrinsic acceptors do not exist and CT via intrinsic defects can be ignored. As soon as electron accepting moiety is incorporated, the PEs can have at least one more competitive decay pathway via CT that can form at least intermediately electrostatically bound electron and hole pairs. The electron and hole pairs can be either bimolecularly recombined to form GSs again or separately transported to each counter electrode in a device. However, in single-layer samples being general for TAS, the CT population has to return to GS bimolecularly due to the lack of an externally connected circuitry. That is the reason why  $J_{SC}$ , a device property, cannot be easily compared with any spectroscopic data without a device structure, although  $J_{SC}$ , often referred as a measure of CC photogeneration probability due to its short-circuit condition. In other words, even for measuring  $J_{SC}$ , the photogenerated electrons have to travel

through the active layer and survive to be detected by a proper external electronic device.

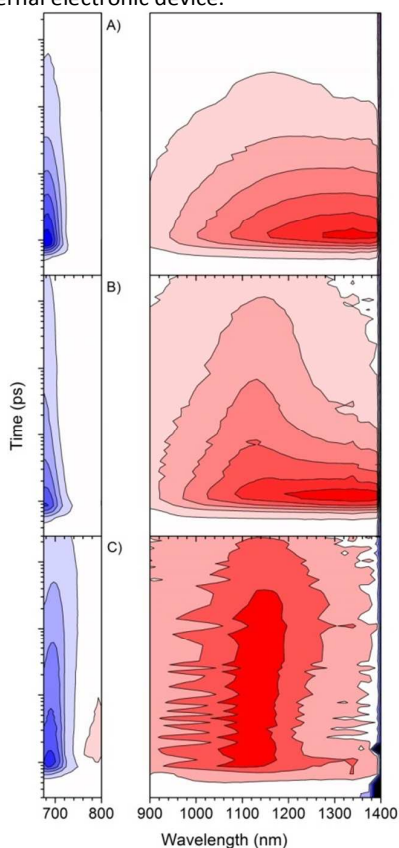


**Figure 5.** 3D contour-type TAS maps with three different acceptor concentrations; A) 0.01 wt%, B) 3.0 wt%, and C) 60 wt%.

This means that the value for  $J_{SC}$  should include CC transport-related terms and escaping over interfacial area terms as well. The values for the HOMO and LUMO of both materials are taken from the previous works by Liang et al.<sup>33</sup> and He et al.<sup>36</sup> for PTB7 and PC<sub>71</sub>BM, respectively.

In Figure 5, three-dimensionally (3D) combined TAS for three representative cases with the acceptor concentration of A) 0.01 wt%, B) 3.0 wt%, and C) 60 wt% are shown to provide an overview of the whole exciton dynamics with a wide range of acceptor concentrations. On the right side of Figure 5, the IR range, 900–1,400 nm, TA spectra are shown while the visible (Vis) range, 550–800 nm, TA spectra are shown on the left side. The x-, y-, and z-axes for the 3D mapping represent wavelength in linear nanometer scale, time in logarithmic ps scale, and  $\Delta A$  in linear dimensionless scale, respectively. As usual, various peaks and bands of excited species are shown in the IR range while photobleached GS band (GSB) is shown in the Vis range. The TAS of the Vis range is shown only up to the pump beam position for convenience. The sign of IR range bands is positive while that of Vis range bands is negative at the prompt moment of pump beam irradiation. All bands converge toward to zero with time as usual. It is noteworthy that the TAS was measured by using single BHJ active layers on

transparent substrates without any electrodes and buffer layers.

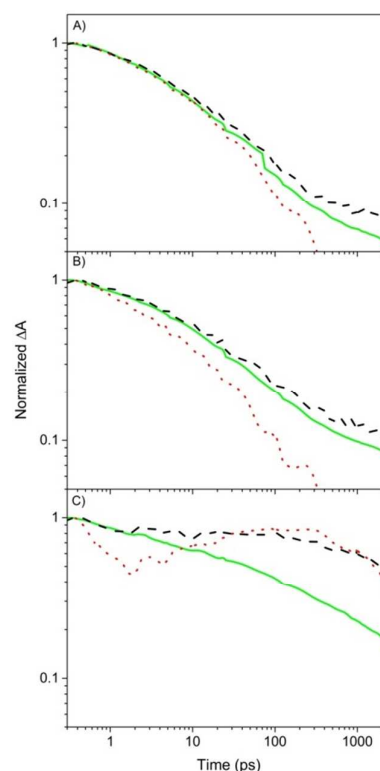


**Figure 6.** Normalized kinetics at various detection wavelengths and acceptor concentrations; A) 0.01 wt%, B) 3.0 wt%, and C) 60 wt%. Straight lines@ 684 nm, dashed lines@ 993 nm, and dotted lines@ 1304 nm.

Therefore, the generated CCs cannot effectively travel through the active layer and extracted by any electrodes as in PV devices; rather, they have to lose their excess energy within the active layer and return to their GSs through various pathways.

3D contour type maps of TAS spectra shown in Figure 5 are raw data without any de-chirping correction. De-chirping treatment is performed for all kinetic data for better accuracy, especially at almost prompt time range of 1–3 ps.

There are strong acceptor concentration-dependent TAS features. First, the broad IR band centered at about 1,350 nm and pronounced at low acceptor concentration was transferred to a band center at about 1,100 nm upon increasing acceptor concentration. Second, the width of the IR band became narrower after transfer. Third, the IR band at the higher acceptor concentration showed clear spectral relaxation feature as reported previously.<sup>22</sup> This is also clearly observable for the Vis range band in Figure 5 C). Fourth, the recovery time of the GSB is extended with increasing acceptor concentration as the second IR band's lifetime is extended.

From the first and second observations, the IR band centered at about 1,350 nm could be assigned as a PE band while the IR

band centered at about 1,100 nm could be assigned as an acceptor-induced band, often referred as CT band.

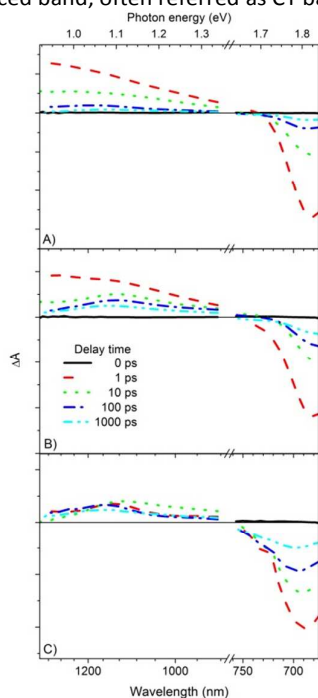


**Figure 7.** TAS spectra of three different acceptor concentrations; A) 0.01 wt%, B) 3.0 wt%, and C) 60 wt% at various delay times of approximately 0, 1, 10, 100, and 1,000 ps.

Then the Vis band centered at about 680 nm could be assigned as a GS band, also due to the opposite sign of  $\Delta A$  compared to the PE and GT bands. This BHJ solid system has an unusual benefit for TAS due to very low PLQYs because strong emission bands can overlap partly with GS and/or with IR bands. This overlap often makes kinetic traces more complex. The third and fourth features reflect that the PE band and the CT band are the major kinetic components through which the native GS population is recovered and is also shown with kinetic traces in Figure 6. Hence, it is strongly suggested that there are no significant needs to consider any other additional processes except the PE, CT, and GS bands population and de-population processes, as depicted in Scheme 1.

In Figure 7, TAS spectra at various delay times of about 0, 1, 10, 100, and 1,000 ps for three different acceptor concentrations, A) 0.01 wt%, B) 3.0 wt%, and C) 60 wt% are shown in energy scale to show their timely evolution in a more quantitative manner. As mentioned in Figure 5, the acceptor concentration-dependent CT is clearly seen again in Figure 6. However, the entire PE band cannot be recorded using our current set-up, but the PE band seems to have a fairly broad FWHM of approximately 0.5 eV compared to the CT band's FWHM of approximately 0.2 eV, if the bands can be assumed as symmetric Gaussian shapes. The broad FWHM of the PE band should be the reason for the lower intensity of the PE band compared to the GS band. Actually, the spectra of A), B), and C) were scaled to have the same initial GS band intensity

as an initial PE population criteria presented with dashed lines in the Vis area of each plot. Due to this normalization with the initial de-population amount of GS, the systematic reduction of PE upon increasing the acceptor concentration can be clearly recognized. It is also remarkable that the CT population, i.e. the CT band intensity, at 3 wt% is already very similar to that at 60 wt%.

This feature will be discussed more in detail with kinetic traces presented in the next part.

In Figure 6, normalized TAS kinetics at various detection wavelengths for the acceptor concentration of A) 0.01 wt%, B) 3.0 wt%, and C) 60 wt% were shown. The TA kinetic decays for the data in Figure 6 were recorded with the same medium excitation intensity described in the experimental part. The first point to notice is that the deviation between PE and CT kinetics are increasing with increasing acceptor concentration. Indeed, the deviation between PE and CT kinetics was not intensely observed at 0.01 wt% as expected. In addition, GSB recovering kinetics at 0.01 wt% was almost the same as both PE and CT kinetics, except below 0.2 in the normalized  $\Delta A$  scale.

In principal, the CT band may not appear at the prompt moment because the CT band is a subsequent population after forming of the PE population. However, PE and CT kinetics seem very similar, especially at low concentration because the PE band's FWHM is extremely broad as this could cover even the whole CT band area as shown in Figure 5 and 7. Hence, CT and PE band kinetics cannot easily be traced independently. Nevertheless, the deviation of TAS kinetics between PE and CT at 3 wt% seems enhanced notably.

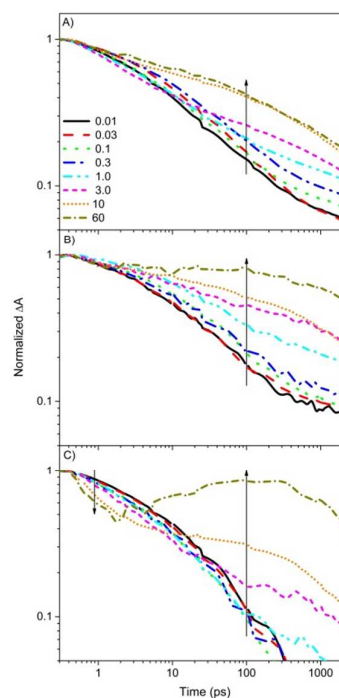


**Figure 8.** Normalized kinetics detected at A) 684 nm, B) 993 nm, and C) 1,304 nm of film samples with various acceptor concentrations, from 0.01 wt% to 60 wt%.

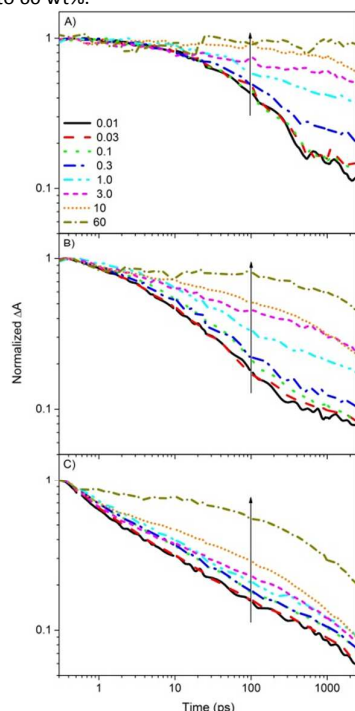


**Figure 9.** Normalized intensity-dependent kinetics detected at 993 nm of film samples with various acceptor concentrations, from 0.01 wt% to 60 wt%. A) Low intensity @  $30 \mu\text{J}/(\text{pulse}\cdot\text{cm}^2)$ , B) medium intensity @  $80 \mu\text{J}/(\text{pulse}\cdot\text{cm}^2)$ , and C) high intensity @  $200 \mu\text{J}/(\text{pulse}\cdot\text{cm}^2)$ .

At 60 wt%, the deviation seems more enhanced; the shortening of lifetime at the initial stage should be a result of acceptor-induced PE depopulation and the slightly delayed rising of kinetic features should be explained with the subsequent population of CT states. To extract statistically stable kinetic parameters in particular for acceptor-induced CT rate constant, wide range of acceptor-concentration dependent TAS were also performed and presented in Figure 8. From Figure 6, the following qualitative conclusions can be drawn; first, basic PE decay lifetime should be about 100 ps; second, subsequent acceptor concentration-dependent PE quenching being correlated with CT population should be much faster than PE lifetime; third, the final process, namely CT decay lifetime, possibly via bimolecular recombination, should have much slower lifetime than PE lifetime as shown in Figure 6 C).

However, the PE kinetic curves significantly deviate from a typical exponential function, mainly due to pronounced bimolecular decay term especially at high excitation intensity depicted with the intensity dependence results in Figure 9.

It is crucial to discuss the excitation intensity-dependent influence on TAS kinetics in particular to avoid mixing of an additional bimolecular exciton decay term, e.g., singlet-singlet annihilation.<sup>37</sup> Avoiding too intense excitation is also important

to prevent any damages on the investigating films due to relatively long and severe TAS measurement condition mainly to improve the small S/N. Although a great amount of information about wide-range excitation intensity-dependent exciton decay behaviors is crucial to expand the knowledge about novel functional materials, a detailed discussion about the incident photon flux-dependent bimolecular behavior is strictly limited to checking the validity of the obtained TAS kinetics, which is requisite for the explanation of essential PV phenomena.

As shown in Figure 9, the most impressive influences upon the reduction of excitation intensity to the kinetics traced at 993 nm are as follows: first, the extension of lifetimes regardless of acceptor concentration and the excited species, i.e., PE and CT, and second, all kinetic traces of low acceptor concentration samples recover their exponential decay functionality from power-law functionality with a slope of about  $-0.5$  at high excitation intensity. It is evident that the exciton dynamics within PTB7:PC<sub>71</sub>BM thin films are highly sensitive to excitation intensity; thus, PE population, and therefore bimolecular processes are dominant at higher intensity compared to other decay processes.

It might be helpful to compare the excitation intensity of the laser pulse with the conventional 1-sun power of  $1 \text{ kW}/\text{m}^2$ , which is a standard for PV operation as well as steady-state characterization.<sup>37</sup> However, serious differences can be noticed on comparing the steady-state continuous-wave (cw) condition directly with the pulsed TAS experimental condition. Assuming the excitation intensity was  $30 \mu\text{J}/(\text{pulse}\cdot\text{cm}^2)$  with the beam diameter of 1 mm at 1 kHz repetition rate, the total incident energy per second on square meter was about  $0.3 \text{ kJ}/(\text{s}\cdot\text{m}^2)$ . Although the value of  $30 \mu\text{J}/(\text{pulse}\cdot\text{cm}^2)$  was the lowest available intensity to obtain reasonable S/N with the equipment used here, the converted incident energy is already comparable to that of standard 1-sun condition. In addition, pulsed TAS has different spectral distribution due to the use of highly monochromated laser beam source compared to conventional white light sources for PV application. Furthermore, if the difference between 100 fs pulse operating of TAS and continuous 1-sun intensity of steady-state operation is compared, then the difference of photon flux density at the impact moment of pump beam is enormous. Hence, applying the kinetic data from conventional pulsed TAS to understand normal operating situation needs significant attention as expected. One additional significant difference might be the fact that the pulsed kinetic situation is governed by the nonequilibrium condition probed by the spectral relaxation as shown in Figure 5 while the steady-state situation should be dominated by the equilibrium condition. The spectral relaxation within conjugated solid systems was intensively discussed by using Kohlrausch-Williams-Watt-type stretched exponential.<sup>28</sup>

In order to extract the reliable PE's native lifetime, kinetic curves detected at 1,304 nm with low excitation intensity for 0 wt% and 0.01 wt% samples were used and the value of extracted TAS PE lifetime was about 85 ps as shown in Table 2. Thus, the lifetime values in Table 2 taken at the  $1/e$  position of

the normalized  $\Delta A$  value was corrected to 100 ps according to the analysis of intensity dependence of the kinetics as plotted in Figure 10 A).

**Table 2.** Overview of TAS kinetic data.

Acceptor concent. (%)	$\tau_{PE@H}$ (/ps)	$\tau_{PE@M}$ (/ps)	$\tau_{PE@L}$ (/ps)
0.01	5.2	14.4	85
0.03	5.2	13.0	74
0.1	4.2	10.6	49
0.3	4.6	10.5	49
1	3.9	10.3	28
3	4.2	8.0	12
10	2.5	3.0	6.0
60	1.5	2.0	1.7

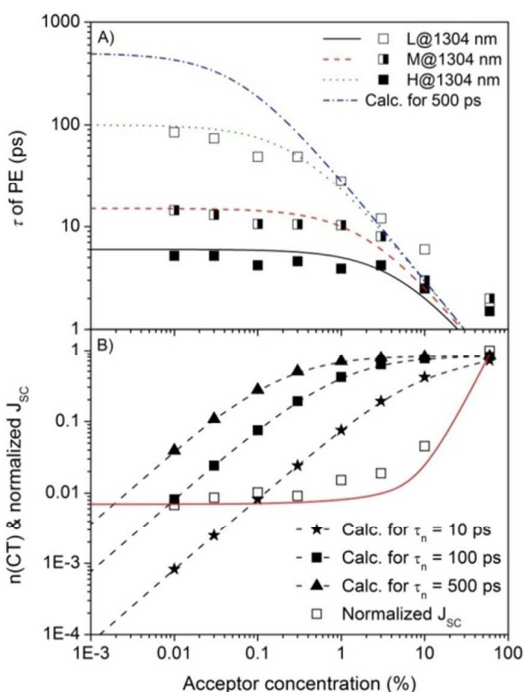


**Figure 10.** A) Acceptor concentration-dependent lifetimes of PE for various excitation intensities and B) Comparison between normalized experimental  $J_{sc}$ , calculated  $n(CT)$ , and calculated  $J_{sc}$  for various lifetimes of native PE decays. The dashed lines are for eye guiding purpose and the straight line is for calculated  $J_{sc}$ .

As the next step, acceptor-induced quenching rate constant could be extracted by using the experimental  $1/e$  lifetimes with a simple kinetic model.  $k_q$  was extracted by fitting the experimental data with Equation (1) being modified slightly for lifetime instead of PLQY. The obtained  $k_q$  was used to plot the model functions as depicted in Figure 10 A). This value was

also used to perform numerical calculations to obtain theoretical kinetic curves based on the model summarized in Scheme 1, as shown in Figure 11.

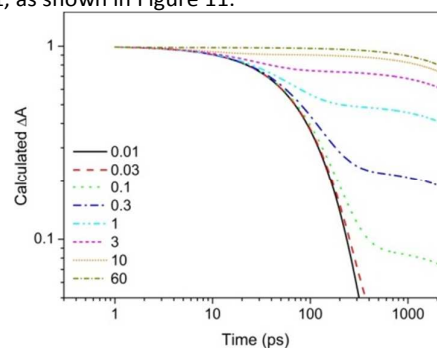


**Figure 11.** Numerically calculated TAS kinetics.

In order to verify the kinetic data with the model shown in Scheme 1, the extracted spectroscopic parameters were used to calculate theoretical kinetic curves by means of a numerical method with Equation (2) and (3).

$$\frac{d[PE]_i}{dt} = (1 - (k_Q \cdot [Q] + k_0)) \cdot [PE]_{i-1} \quad (2)$$

$$\frac{d[CT]_i}{dt} = (1 - k_{CC}) \cdot [CT]_{i-1}, \quad (3)$$

where  $k_0$  is the rate constant of native PE decay;  $k_{CC}$  is the rate constant of CC generation from the CT band. The iterative procedures were done by a conventional spreadsheet program with 1 ps time interval. The used input parameters for calculation shown in Figure 11 were  $1 \times 10^{10} \text{ s}^{-1}$  for  $k_n$ ,  $3.3 \times 10^{12} \text{ s}^{-1}$  for  $k_Q$ , and  $1 \times 10^8 \text{ s}^{-1}$  for  $k_{CC}$ . The corresponding lifetimes that were reciprocally related to rate constants were 100 ps, 0.3 ps, and 10 ns, respectively. Actually,  $k_0$  is a combination of all decay channels related to direct PE depopulation, e.g., nonradiative and radiative decay without extrinsic depopulation such as the acceptor-induced CT process. However, the rate constant for radiative decay was not explicitly added for theoretical calculation because this may not affect the major character of the PE decay rate constant as the PLQY of a pristine film of PTB7 is only 2.2%. It is informed that Figure 10 is for the same time range with the experimental TAS results for comparison and another plot for a longer time range is shown in the supplementary information part as Figure S1.

Interestingly, the acceptor concentration-dependent quenching rate constant of  $1.5 \times 10^{13} \text{ s}^{-1}$  extracted from the PLQY, especially at low concentration shown in Figure 2 is about 6-fold faster than that of  $3.3 \times 10^{12} \text{ s}^{-1}$  extracted from the systematic shortening of PE's lifetimes over a wide range of acceptor concentrations shown in Figure 8. However, the rate constant of  $3.2 \times 10^{12} \text{ s}^{-1}$  for the PPV:TNF system and that extracted with PLQY for a higher concentration range in this study seem reasonably comparable. All of those trends have a deviation from linear dependency relation at higher concentration, i.e., the lowering of  $k_Q$ . This lowering of PLQY

with the PTB7 case seems analog to a phenomenon of an increase of PL due to the bigger domain size after annealing of the P3HT:PC<sub>61</sub>BM system<sup>38</sup> in addition to its extremely low PLQY values discussed before with Figure 2.

Considering the difference of molecular weights (MWs) of TNF (315.19 g/mol) and PC<sub>71</sub>BM (1030.99 g/mol), a TNF molecule has only about 1/3 of weight compared to a PC<sub>71</sub>BM molecule. Consequently, about 30% shortening of the average intermolecular distance for TNF at the same wt% concentration is expected by using a simple cubic lattice arrangement assumption. Thus, it can be concluded that PC<sub>71</sub>BM has more efficient quenching capability under homogeneously dispersed situation at lower concentrations than smaller TNF and PDI acceptors. This can be one of the reasons for the higher PCE of organic BHJ solar cells with a fullerene derivative in addition to their morphology and electronic benefits.

As shown in Figure 11, the calculated kinetic curves have comparable functional dependence with the experimental kinetics as shown in Figure 9 A). These curves are combinations of PE and CT kinetic curves for each acceptor concentration in order to simulate experimental kinetic curves traced at 993 nm at low excitation intensity due to a broad PE band. Actually, the model calculation for Figure 11 had to include a bimolecular decay term in order to include the power-law decay character at high excitation intensity as shown in Figure 9 C). In addition, a spectral relaxation term has to be implied in a proper way, for instance, by adapting a stretched exponential term to correct nonequilibrium behavior of PE in the solid system. However, additional terms for bimolecular decay and spectral relaxation were not explicitly included here in order to keep the model as simple as possible. In this study, only the experimental PE lifetime was slightly extended to include the fact that the kinetics without serious excitation intensity condition should have more pronounced exponential functionality. For that, the extracted native 1/e lifetimes with various excitation intensities as listed in Table 2 were compared and increased about 18%, from 85 ps to 100 ps, also for simplicity.

To compare the calculated and measured kinetic curves at a glance,  $k_n$  of 100 ps for the kinetic calculation seems shorter than it should be, especially at the initial time range. However, the tail parts of the experimental kinetic curves, where  $\Delta A$  is reduced to approximately 20% compared to their initial value, were significantly extended. This feature should be correlated with stretched exponential behavior being pronounced in a broad density-of-states (DOS) being typical for disordered solid systems. Such disorder is often referred as a needed condition for energetic down-hill migrations of excited species, and can be observed as spectral relaxation shown in Figure 5 C). Therefore, only moderately extended value of 100 ps was chosen as a reliable compromise of  $k_n$  to simulate the model kinetics.

In Figure 10 A), PE decay lifetimes at various excitation intensities listed in Table 2 were shown. Interestingly, all of the lifetimes at the high acceptor concentration range were linearly shortened and converged to a common value. Therefore, theoretical calculation could be done by using the

same  $k_Q$  independent of excitation intensity. The characteristic plateau regions that lowered with increasing excitation intensity were also observed. The lowering of the plateau is shortening of PE lifetimes due to intense bimolecular decay up to a certain acceptor concentration at a given intensity. This means that the PEs readily undergo bimolecular decay very effectively rather than acceptor-induced decay when the PE population is high. In addition, the wider average distance between acceptors at a lower acceptor concentration provides results in more probability of the photogenerated PEs to interact with each other before they can reach to any acceptors at the initial decay phase. To simulate low excitation intensity in order to explore usual photon flux situation for ordinary PV operation, a theoretical trend curve for low excitation intensity was calculated with a PE lifetime of 500 ps and is presented in Figure 10 A). By using the data of 1 wt% in Table 2, a linearly decreasing relation can be observed for lifetimes as a function of excitation intensity, while the functional dependencies are super-linear with acceptor concentration lower than 1 wt% and sublinear with acceptor concentration higher than 1 wt%. Indeed, the bimolecular decay effect is taken into account by subtracting a constant value from  $t_n$  for each excitation intensity. This is a practical method as shown but should have limitation as a rough approximation because of the complicated exciton dynamics in disordered BHJ solid systems.

In Figure 10 B), the total number of CT population, assigned as  $n(\text{CT})$ , obtained by integrating all generated CTs with various native PE lifetimes are plotted as functions of [Q]. The calculations were done with various values of  $t_n$  in order to correct the bimolecular effects eventually caused by high excitation intensity. In order to compare  $n(\text{CT})$  with  $J_{\text{SC}}$ ,  $n(\text{CT})$  was multiplied with the value of conductivity converted by the experimentally obtained  $R_s$  and this should be proportional to a extracting probability of CCs from an active layer to an external circuitry. Finally,  $n(\text{CT})$  and the total number of detected CCs, assigned as  $n(\text{CC})$ , can be compared to disentangle the quantitative relation between CT and CC, in other words, spectroscopic kinetics and electronic device property. For Figure 10 B),  $J_{\text{SC}}$  was used to compare with the spectroscopic results because  $J_{\text{SC}}$  is the photocurrent of a PV device at an external electric field of 0 V. Therefore,  $J_{\text{SC}}$  can be regarded as the number of photogenerated and detectable CCs being more similar to the character of CT detected with TAS than the number of CCs collected at maximum power point condition.

However, it seems that the experimental  $J_{\text{SC}}$  and the calculated  $n(\text{CT})$  have dramatic differences in their functional dependencies as shown in Figure 10 B). For lower excitation intensity only for hypothetical calculation with 500 ps  $t_n$ , the calculated IQEs of CT are 82% for 10 wt% [Q] and 83% for 60 wt% [Q]. A plausible explanation for the discrepancy can be based on the fact that the CCs cannot fully escape from the inside of an active layer to the electrodes, especially at low acceptor concentration as many groups have reported that the CC mobility as well as the PCE is much improved via proper phase separation at high acceptor concentration, mostly at

about 60 wt%. Actually, our previous study about the thickness-dependent IQE by using same PTB7 BHI system<sup>20</sup> has shown decreasing IQE with increasing active layer thickness. This reflects that the numbers of safely extracted CCs decrease with increasing thickness although the PE generation efficiency should not be affected by the increasing thickness.

The values of  $n(\text{CT})$  are approximately 76% for 10 wt% [Q] and 82% for 60 wt% [Q] with the lowest experimental excitation intensity used in this study. For this condition, the used  $t_n$  was 100 ps. The IQE obtained with a 90 nm-thick device was about 70–80% over the entire absorption spectral range with a 60 wt% device.<sup>20</sup> As the same thickness of 100 nm was used for all the samples in this study, it can be concluded that the generated CTs mostly survive by escaping from the active layer to electrodes, except approximately 20–30% of the whole PE population. It is clear that the 20–30% loss is nothing but the portion of PEs dissipated to GS via native unimolecular direct decays. The conclusion can be simplified and expressed as Equation (4) and (5).

$$n(\text{PE}) - n(\text{DD}) = n(\text{CT}) \quad (4)$$

$$n(\text{CT}) - n(\text{BR})(d) = \text{extracted } n(\text{CC}) \quad (5)$$

where DD stands for direct monomolecular decay from PE. In this study, DD is a combination of R and NR terms as depicted in Scheme 1. However, the additional loss is increasing with increasing active layer thickness as shown previously<sup>24</sup> probed by the decreasing of IQE with increasing active layer thickness. Therefore, the number of BR is written as a function of active layer thickness as  $n(\text{BR})(d)$  in Equation (5).

From that conclusion, we have to correct our previous conclusion that the CC collecting probability of the approximately 100 nm-thick active layer is almost 100% rather than the approximate 70% given in the previous study<sup>24</sup> because the 30% loss is not caused from CC or CT but from PE through direct native decay. Consequently, it should be concluded that the already-formed acceptor-induced CTs are possible to form CCs without any significant loss and subsequently the CCs can also be transported without any significant loss, especially at a relatively thin active layer condition except the DD loss of PE. Differently expressed, the CC-collecting probability at <100 nm thickness is about 100% without any meaningful bimolecular recombination losses.

## Conclusions

In this study, PTB7 thin films blended with acceptor, PC<sub>71</sub>BM, including a wide range of low acceptor concentration were investigated by means of TAS. From the obtained acceptor concentration-dependent kinetic data, PTB7's native spectroscopic lifetime of approximately 100 ps in conjunction with the acceptor-induced CT rate constant of approximately  $3.3 \times 10^{12} \text{ s}^{-1}$  were extracted. Furthermore, a CT decay lifetime of about 10 ns was extracted from the TAS kinetic data. These results were examined by performing a numerical simulation based on the suggested kinetic model. The conceptual model

seems enough to reconstruct all important dependent functions as a function of acceptor concentration.

Finally, the spectroscopic data were compared with device properties, in particular  $J_{\text{SC}}$  and previously estimated IQEs of PTB7 BHI systems. By adapting experimentally estimated conductivity as a converting as well as escaping probability of  $n(\text{CT})$  to detectable  $n(\text{CC})$ , it seems that most CT populations were converted to CC without any significant loss. Therefore, it can be concluded that most CT can be extracted as CC bimolecular recombination loss freely in an optimized device with high blending ratio of about 60 wt% and thin active layer thickness of about 100 nm.

It is noteworthy that this study is needed to be extended to the acceptor concentration range close to the conventional preparation range, from 10% to 80%, in order to confirm the suggested model shown in figure 10 more firmly as well as the concentration range where the acceptor portion is significantly dominated to enhance current understanding of the semiconducting polymer blend systems.

## Acknowledgements

This study was supported by the Konkuk University in 2014.

## References

- Z. He, C. Zhong, X. Huang, W.-Y. Wong, H. Wu, L. Chen, S. Su and Y. Cao, *Adv. Mater.*, 2011, **23**, 4636.
- K. Zhang, K. Gao, R. Xia, Z. Wu, C. Sun, J. Cao, L. Qian, W. Li, S. Liu, F. Huang, X. Peng, L. Ding, H.-L. Yip, and Y. Cao, *Adv. Mater.*, 2016, **28**, 4817-4823.
- Z. Xiao, X. Geng, D. He, X. Jia and L. Ding, *Energy Environ. Sci.*, 2016, **9**, 2114-2121.
- F. C. Krebs, N. Espinosa, M. Hösel, R. R. Søndergaard and M. Jørgensen, *Adv. Mater.*, 2014, **26**, 29-39.
- C. Im, J. M. Lupton, P. Schouwink, S. Heun, H. Becker and H. Bässler, *J. Chem. Phys.*, 2002, **117**, 1395.
- D. Jarzab, F. Cordella, J. Gao, M. Scharber, H.-J. Egelhaaf and M. A. Loi, *Adv. Energy Mater.*, 2011, **1**, 604-609.
- H. Ohkita and S. Ito, *Polym.*, 2011, **52**, 4397-4417.
- A. Armin, I. Kassal, P. E. Shaw, M. Hamsch, M. Stolterfoht, D. M. Lyons, J. Li, Z. Shi, P. L. Burn and P. Meredith, *J. Am. Chem. Soc.*, 2014, **136**, 11465-11472.
- S. Cook, A. Furube and R. Katoh, *Energy Environ. Sci.*, 2008, **1**, 294-299.
- T. Clarke, A. Ballantyne, F. Jamieson, C. Brabec, J. Nelson and J. Durrant, *Chem. Commun.*, 2009, **89**, 89-91.
- O. V. Mikhnenko, H. Azimi, M. Scharber, M. Morana, P. W. M. Blom and M. A. Loi, *Energy Environ. Sci.*, 2012, **5**, 6960.
- R. Tautz, E. Da Como, T. Limmer, J. Feldmann, H.-J. Egelhaaf, E. von Hauff, V. Lemaury, D. Beljonne, S. Yilmaz, I. Dumsch, S. Allard and U. Scherf, *Nat. Commun.*, 2012, **3**, 970.
- G. Grancini, D. Fazzi, M. Binda, M. Maiuri, A. Petrozza, L. Criante, S. Perissinotto, H.-J. Egelhaaf, D. Brida, G. Cerullo and G. Lanzani, *Proc. of SPIE* 2013, **8811**, 88111D.
- X. Guo, N. Zhou, S. J. Lou, J. Smith, D. B. Tice, J. W. Hennek, R. P. Ortiz, J. T. L. Navarrete, S. Li, J. Strzalka, L. X. Chen, R. P. H. Chang, A. Facchetti and T. J. Marks, *Nature Photonics*, 2013, **10**, 1038.
- W. Zhang, Y. Huang, Y.-D. Xing, Y. Jing, L. Ye, L.-M. Fu, X.-C. Ai, J.-H. Hou and J.-P. Zhang, *Opt. Express*, 2013, **21**, A241.
- L. G. Kaake, Y. Sun, G. C. Bazan and A. J. Heeger, *Appl. Phys. Lett.*, 2013, **102**, 133302.

- 17 Y.-J. Cheng, S.-H. Yang and C.-S. Hsu, *Chem. Rev.*, 2009, **109**, 5868-5923.
- 18 M. C. Scharber and N.S. Sariciftci, *Prog. Polym. Sci.*, 2013, **38**, 1929-1940.
- 19 B. Carsten, J. M. Szarko, H. J. Son, W. Wang, L. Lu, F. He, B. S. Rolczynski, S. J. Lou, L. X. Chen and L. Yu, *J. Am. Chem. Soc.*, 2011, **133**, 20468-20475.
- 20 Y. W. Soon, H. Cho, J. Low, H. Bronstein, I. McCulloch and J. R. Durrant, *Chem. Commun.*, 2013, **49**, 1291.
- 21 G. J. Hedley, A. J. Ward, A. Alekseev, C. T. Howells, E. R. Martins, L. A. Serrano, G. Cooke, A. Ruseckas and I. D. W. Samuel, *Nat. commun.*, 2013, **4**, 2867.
- 22 J. M. Szarko, B. S. Rolczynski, S. J. Lou, T. Xu, J. Strzalka, T. J. Marks, L. Yu and L. X. Chen, *Adv. Funct. Mater.*, 2014, **24**, 10.
- 23 Marina Gerhard, Andreas P. Arndt, Ian A. Howard, Arash Rahimi-Iman, Uli Lemmer and Martin Koch, *J. Phys. Chem. C*, 2015, **119**, 28309-28318.
- 24 H. Park, J. An, J. Song, M. Lee, H. Ahn, M. Jahnel and C. Im, *Sol. Energy Mater. Sol. Cells*, 2015, **143**, 242-249.
- 25 P. J. Brown, D. S. Thomas, A. Köhler, J. S. Wilson, J. S. Kim, C. M. Ramsdale, H. Sirringhaus and R. H. Friend, *Phys. Rev. B*, 2003, **67**, 064203.
- 26 P. Qin, G. Fang, N. Sun, X. Fan, Q. Zheng, F. Chen, J. Wan and X. Zhao, *Appl. Surf. Sci.*, 2011, **257**, 3952.
- 27 U. Rösch, S. Yao, R. Wortmann and F. Würthner, *Angew. Chem. Int. Ed.*, 2006, **45**, 7026.
- 28 B. Mollay, U. Lemmer, R. Kersting, R. F. Mahrt, H. Kurz, H. F. Kauffmann and H. Bässler, *Phys. Rev. B*, 1994, **50**, 10769.
- 29 H. Yi, C. Im, J. An, S. Lee and H. Park, *J. Kor. Phys. Soc.*, 2014, **64**, 910-916.
- 30 J. A. Bartelt, Z. M. Beiley, E. T. Hoke, W. R. Mateker, J. D. Douglas, B. A. Collins, J. R. Tumbleston, K. R. Graham, A. Amassian, H. Ade, J. M. J. Fréchet, M. F. Toney and M. D. McGehee, *Adv. Energy Mater.*, 2013, **3**, 364-374.
- 31 C. Im, E. V. Emelianova and H. Bässler, *J. Chem. Phys.*, 2002, **117**, 2961.
- 32 A) P. Atkins and J. de Paula, *Physical Chemistry*, 9th edition, Oxford University Press, 2010, p 819.; B) J. R. Lakowicz, *Principles of Fluorescence Spectroscopy*, 2nd edition, Kluwer Academic / Plenum Publishers, 1999, p 239.
- 33 Y. Liang, Z. Xu, J. Xia, S.-T. Tsai, Y. Wu, G. Li, C. Ray and L. Yu, *Adv. Mater.*, 2010, **22**, E135-E138.
- 34 C. Im, W. Tian, H. Bässler, A. Fechtenkötter, M. D. Watson and K. Müllen, *J. Chem. Phys.*, 2003, **7**, 119.
- 35 Z. He, C. Zhong, S. Su, M. Xu, H. Wu and Y. Cao, *Nat. Photonics*, 2012, **6**, 591-595.
- 36 C. J. Brabec, V. Dyakonov, N. S. Sariciftci, W. Graupner, G. Leising and J. C. Hummelen, *J. Chem. Phys.*, 1998, **109**, 15.
- 37 A) C. Honsberg and S. Bowden, Part 2. Properties of Sunlight, <http://www.pveducation.org/pvc/drom/properties-of-sunlight/>; B) C. Honsberg and S. Bowden, part 8. Characterization, <http://www.pveducation.org/pvc/drom/characterisation/>.
- 38 U. Zhokhavets, T. Erb, H. Hoppe, G. Gobsch and N. S. Sariciftci, *Thin Solid Films*, 2006, **496**, 679-682.